

Multi-level Asymmetric Contrastive Learning for Volumetric Medical Image Segmentation Pre-training

Shuang Zeng, Lei Zhu, Xinliang Zhang, Qian Chen, Hangzhou He, Lujia Jin, Zifeng Tian, Qiushi Ren, Zhaoheng Xie, Yanye Lu

Abstract—Medical image segmentation is a fundamental yet challenging task due to the arduous process of acquiring large volumes of high-quality labeled data from experts. Contrastive learning offers a promising but still problematic solution to this dilemma. Because existing medical contrastive learning strategies focus on extracting image-level representation, which ignores abundant multi-level representations. And they underutilize the decoder either by random initialization or separate pre-training from the encoder, thereby neglecting the potential collaboration between the encoder and decoder. To address these issues, we propose a novel multi-level asymmetric contrastive learning framework named MACL for volumetric medical image segmentation pre-training. Specifically, we design an asymmetric contrastive learning structure to pre-train encoder and decoder simultaneously to provide better initialization for segmentation models. Moreover, we develop a multi-level contrastive learning strategy that integrates correspondences across feature-level, image-level, and pixel-level representations to ensure the encoder and decoder capture comprehensive details from representations of varying scales and granularities during the pre-training phase. Finally, experiments on 12 volumetric medical image datasets indicate our MACL framework outperforms existing 11 contrastive learning strategies. *i.e.* Our MACL achieves a superior performance with more precise predictions from visualization figures and 2.28%, 1.32%, 1.62% and 1.60% Average Dice higher than previous best results on CHD, MMWHS, CHAOS and AMOS, respectively. And our MACL also has a strong generalization ability among 5 variant U-Net backbones. Our code will be available at <https://github.com/stevezs315/MACL>.

Index Terms—Medical Image Segmentation, Self-supervised Learning, Contrastive Learning

I. INTRODUCTION

This work was supported in part by the Natural Science Foundation of China (82371112, 623B2001, 62394311), in part by Beijing Municipal Natural Science Foundation (Z210008). (Corresponding author: Yanye Lu.)

Shuang Zeng, Lei Zhu, Xinliang Zhang, Qian Chen, Hangzhou He, Lujia Jin, Zifeng Tian, Qiushi Ren, Zhaoheng Xie and Yanye Lu are with the Institute of Medical Technology, Peking University Health Science Center, Peking University, Beijing 100191, China, also with the Department of Biomedical Engineering, Peking University, Beijing 100871, China, also with the National Biomedical Imaging Center, Peking University, Beijing 100871, China, also with the Institute of Biomedical Engineering, Shenzhen Bay Laboratory, Shenzhen 5181071, China, and also with the Institute of Biomedical Engineering, Peking University Shenzhen Graduate School, Shenzhen 518055.

MEDICAL image segmentation, defined as the partition of the entire image into different tissues, organs or other biologically relevant structures, plays a critical role in the computer-aided diagnosis paradigm. Although models with fully supervised training can dramatically improve the performance of segmentation task, it is really a challenge to assemble such large annotated medical image datasets due to the extensive and burdensome annotation effort and the requirement of expertise. Meanwhile, substantial unlabeled image data from modalities such as CT and MRI are generated every day all around the world. Therefore, it is highly desirable to propose some methods which can alleviate the following requirement: leveraging numerous unlabeled data to pre-train models and achieve high performance with limited annotations.

Self-supervised learning (SSL) leads a promising direction to this dilemma: it provides a pre-training strategy that relies only on unlabeled data to obtain a suitable initialization for training downstream tasks with limited annotations. In recent years, SSL methods have been highly successful for downstream analysis of not only natural images, but also medical images. As a particular variant of SSL, contrastive learning (CL) [1], [2] has shown great success in learning image-level features from large-scale unlabeled data which greatly reduces annotation costs. In CL framework setting, an encoder is initially pre-trained on unlabeled data to extract valuable image representations. Subsequently, the pre-trained encoder serves as a well-suited initialization for training supervised downstream tasks, such as classification, object detection and segmentation, which can be fine-tuned into an accurate model with additional modules (*e.g.* a decoder for segmentation), even with limited labeled data. Additionally, CL framework requires an appropriate *contrastive loss* [1] to effectively attract similar pair representations (*a.k.a.* positive pairs) and repel dissimilar pair representations (*a.k.a.* negative pairs). This is predicated on the observation that different augmentations of the same image should yield similar representations, while representations derived from distinct images ought to differ.

In terms of medical image segmentation, several medical CL frameworks [3]–[7] in Figure 1(a) and (b) have shown exciting results, which inspire us to excavate the potential of medical CL. Specifically, they pre-train an U-Net encoder along with an image-level projector and image-level contrastive loss to

extract inter-image discrimination. And then they combine the well pre-trained encoder with a randomly initialized decoder for fine-tuning the downstream segmentation task. However, despite its success, there are still some important issues to be solved when applying CL to this specific medical image segmentation task: 1) Medical image segmentation aims to predict the class label for each pixel within one image, which focuses on intra-image discrimination, instead of inter-image discrimination. In this sense, it poses demands for more distinctive pixel-level representation learning, which will be more appropriate for medical image segmentation. However, those medical CL works [3]–[7] focus on extracting image-level projection output from the encoder along with an image-level projector, which do not exploit the luxuriant details of both feature-level projection from the encoder and pixel-level projection from the decoder. Therefore, these pre-trained models can be sub-optimal for segmentation task due to the discrepancy between image-level projection and pixel-level projection and the missing of the implicit feature-level consistency. 2) The symmetric encoder-decoder architecture is widely used for fully supervised medical image segmentation. And due to the downsampling layers of encoder, deconvolutional layers of decoder and skip connections, the encoder-decoder structure can not only effectively extract multi-level representations but also preserve intricate details and edge information within medical images, hence facilitating more precise segmentation of subtle substructures such as tumors and cells. Such an efficient collaborative work paradigm inspires us that incorporating a decoder together with an encoder for CL pre-training should enhance the performance of downstream segmentation task. However, those proposed medical CL frameworks do not make full use of the decoder because their decoder is either randomly initialized and trained during downstream fine-tuning [3]–[6] or pre-trained separately from the encoder, ignoring the collaboration between the encoder and decoder during pre-training [7].

To fill the gap, we propose a novel **Multi-level Asymmetric CL** framework named MACL shown in Figure 1(c) by introducing an asymmetric CL structure and a multi-level CL strategy to realize one-stage encoder-decoder synchronous pre-training. Different from the previous works, there are mainly two characteristics of our proposed framework: 1) We propose a multi-level CL strategy (*i.e. image-level, feature-level, pixel-level*) from global to local to make sure luxuriant details from multi-scale and multi-granularity representations can be learned by the encoder and decoder during pre-training. 2) We incorporate a decoder into normal *one-encoder* CL framework to realize the synchronous encoder-decoder pre-training and further make an adaptive modification to the decoder which finally forms an asymmetric CL structure. Specifically, instead of directly introducing a symmetric encoder-decoder structure to both of the two branches, we introduce an encoder with a partial decoder in the dominant branch while only an encoder in the auxiliary branch. With such an asymmetric structure, our MACL can delightfully reduce the computation complexity of the model and guarantee sufficient negative pairs for CL. According to our experimental results, our proposed MACL outperforms other 11 methods across 12 medical image

datasets. In summary, our main contributions are threefold:

1) A multi-level contrastive learning strategy is designed to take the correspondence among image-level, pixel-level and feature-level projections respectively into account to make sure multi-level representations can be learned by the encoder and decoder during pre-training.

2) In order to get better initialization for the entire downstream segmentation model, our proposed MACL adopts an asymmetric encoder-decoder CL structure, which introduces a partial decoder into the one-stage CL framework and pre-trains the encoder and decoder simultaneously.

3) State-of-the-art results have been achieved across 12 datasets from both CT and MRI for multi-organ segmentation and ROI-based segmentation compared with other 11 CL methods. Further, we also conduct experiments to verify the generalization ability of our proposed MACL and ablation studies to validate the effectiveness of our proposed MACL.

II. RELATED WORKS

A. Medical Image Segmentation

In recent years, deep learning techniques, especially convolutional neural networks (CNNs), have emerged as powerful tools for medical image segmentation. Among those designs, FCN [8], UNet [9] and DeepLab [10] function as three milestones. They and their variants provide a stable and consistent baselines for segmentation tasks. Among the most notable architectures, U-Net [9] stands out for its effective use of encoder-decoder structures and skip connections, enabling precise delineation of anatomical structures. Building upon U-Net's success, attention U-Net [11] incorporates attention gates (AGs) to the skip connections to implicitly learn to suppress irrelevant regions in the input image while highlighting the regions of interest for the segmentation task. Similarly, in order to solve the semantic gaps for an accurate medical image segmentation, UCTransNet [12] proposes a CTrans module to replace the original skip connection, which consists of a sub-module named CCT to conduct the multi-scale channel cross fusion with transformer and another sub-module named CCA to incorporate channel-wise cross-attention. And BCDU-Net [13] incorporates a bi-directional convolutional long-term-short-memory (LSTM) module to combine the feature maps in a non-linear way and the mechanism of dense convolutions to strengthen feature propagation and encourage feature reuse. Additionally, residual U-Net [14] incorporates residual connections to facilitate information flow and alleviate vanishing gradient problems, resulting robust and stable segmentation outcomes. For 3D medical image segmentation, nnUNet [15] accomplishes searching suitable hyper-parameters including augmentations, pre-processing and post-processing techniques, etc. Its pipeline and code-base provide a strong baseline for a broad scope of tasks.

B. Contrastive Learning

As a particular variant of SSL, CL has shown great success in learning image-level features from large-scale unlabeled data which greatly reduces annotation costs, hence serving as a vital role in video frame prediction, semantic segmentation,

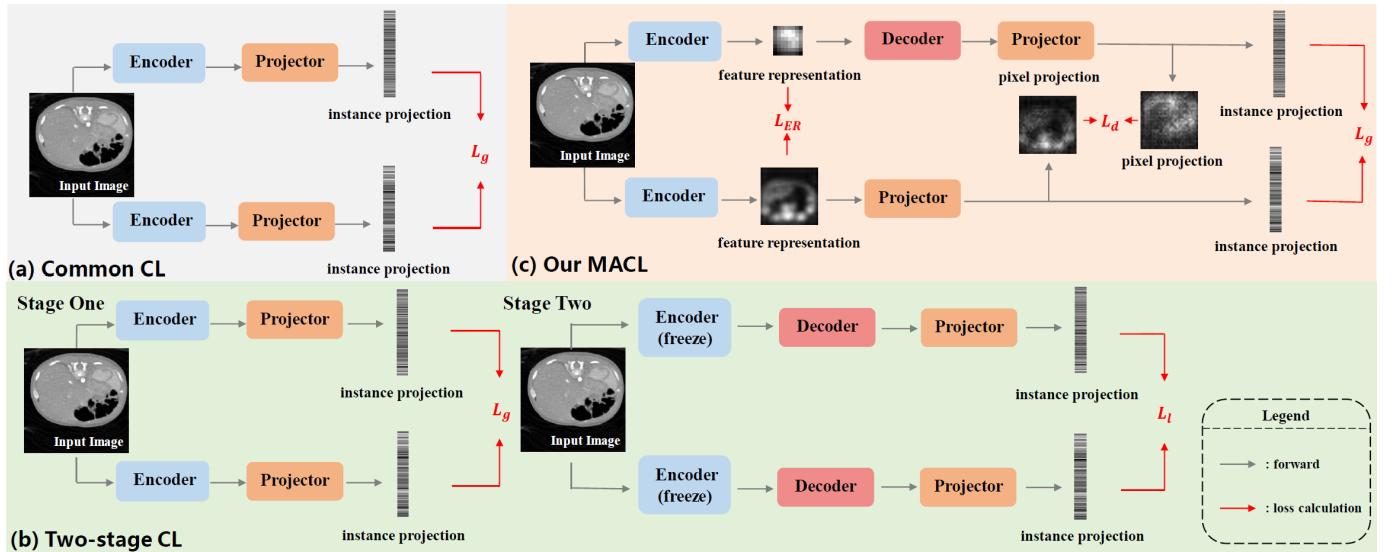


Fig. 1. Comparison of different CL frameworks for medical images: (a) Common CL frameworks used for medical image segmentation are symmetric and similar to SimCLR. (b) Two-stage CL framework pre-trains the encoder with global contrastive loss and decoder with local contrastive loss in separate stage which ignores the collaboration between the encoder and decoder. (c) Our proposed MACL framework is asymmetric with an additional partial decoder for pre-training and integrates multi-level CL strategy including feature-level equivariant regularization, image-level and pixel-level CL to get better initialization of both encoder and decoder for downstream segmentation tasks.

object detection and so on. The core idea of CL is to attract the positive sample pairs and repulse the negative sample pairs through optimizing a model with InfoNCE [16] loss. In practice, CL methods benefit from a large number of negative samples [1], [2]. MoCo [2] introduces a dynamic memory bank to maintain a queue of negative samples. SimCLR [1] employs a substantial batch size to facilitate the coexistence of a significant number of negative samples within the current batch. Beyond the aforementioned classic training framework, SwAV [17] incorporates online clustering into Siamese network and proposes a new ‘multi-crop’ augmentation strategy that mixes the views of different resolutions. BYOL [18] introduces a slow-moving average network and shows that CL can be effective without any negative samples. By introducing stop-gradient, SimSiam [19] shows that simple Siamese networks can learn meaningful representations even without negative pairs, large batches or momentum encoders.

C. Contrastive Learning for Medical Image Segmentation

In the medical imaging domain, substantial efforts of contrastive learning [3]–[7], [20] have been devoted to incorporating unlabeled data to improve network performance due to the limited data and annotations. Researchers mainly focus on the design of siamese networks and construction of contrastive pairs to pre-train the model for several downstream tasks such as medical image classification, segmentation, registration and retrieval. Specifically, in terms of segmentation task, for the design of siamese networks, DeSD [4] reformulates CL in a deep self-distillation manner to improve the representation quality of both shallow and deep sub-encoders to address the issue that SSL may suffer from the weak supervision at shallow layers. DiRA [5] designs a novel self-supervised learning framework by uniting discriminative, restorative and

adversarial learning in a unified manner to glean complementary visual information from unlabeled medical images. For the construction of contrastive pairs, SimTriplet [6] proposes a *triplet-shape* CL framework which maximizes both intra-sample and inter-sample similarities via triplets from positive pairs without using negative samples to take advantage of multi-view nature of medical images. GCL [7] proposes a *partition-based* contrasting strategy which leverages structural similarity across volumetric medical images to divide unlabeled samples into positive and negative pairs and formulates a local version of contrastive loss to learn distinctive local representation used for per-pixel segmentation. PCL [3] further proposes a *position-based* CL framework to generate contrastive data pairs by leveraging the position information in volumetric medical images which can alleviate the problem that simple CL methods and GCL still introduce a lot of false negative pairs and result in degraded segmentation quality due to the circumstance where different medical images may have similar structures or organs.

III. METHODS

This section first defines how to pre-train a model with CL framework for medical image segmentation. Then we propose a novel asymmetric CL structure which can pre-train both encoder and decoder in a single stage. Then, the multi-level contrastive learning strategy of our MACL is discussed to consider multi-level representations. Finally, the experimental setup including datasets and implementation details is described.

A. Problem Definition

Given an input image $\mathbf{X} \in \mathbb{R}^{C_x \times H_x \times W_x}$, medical image segmentation aims to classify pixels in the image with a

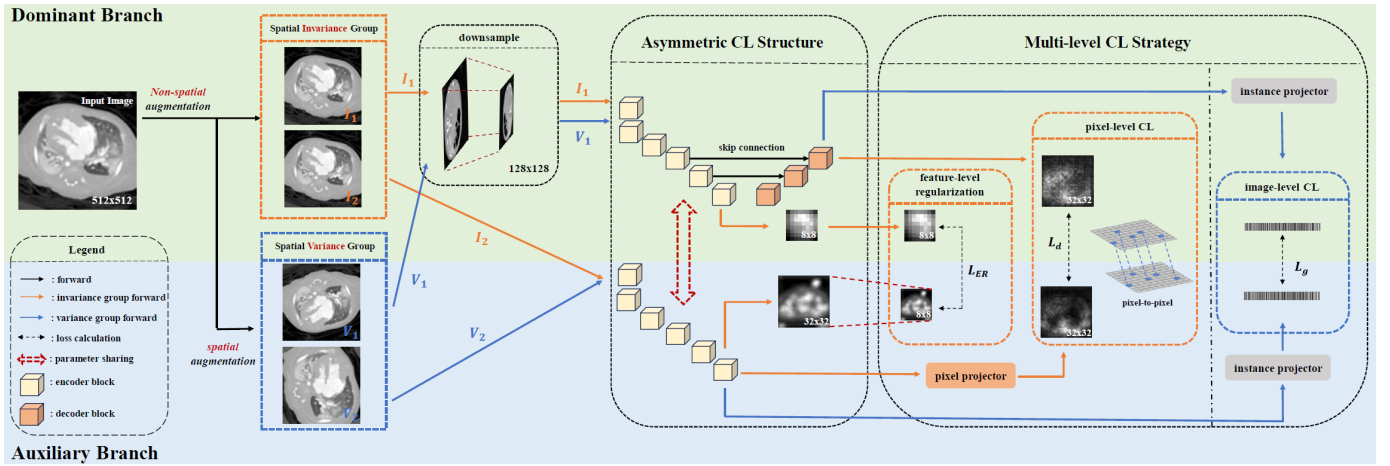


Fig. 2. Overview of our proposed MACL framework. The input image is propagated to two branches: the dominant branch and auxiliary branch. In the dominant branch, after augmentation and downsampling, the input image is fitted into the encoder to get feature-level representation, and then propagated to the decoder and projector to get image-level and pixel-level projections; while in the auxiliary branch, it is the same process but no decoder will be used. The feature-level representations from two branches will be used in equivariant regularization loss, while image-level and pixel-level projections will be used in global and dense contrastive loss, respectively to achieve multi-level contrastive learning.

segmentation network, where $H \times W$ is the resolution of the image, C denotes the number of channels. To achieve this purpose, the segmentation network needs an encoder $e(\cdot)$ to extract multi-level features and then a decoder $d(\cdot)$ is used to fuse the features into $Z \in \mathbb{R}^{C_z \times H_z \times W_z}$ to recover image details:

$$Z = d(e(\mathbf{X})) = d(\{\mathbf{X}^1, \mathbf{X}^2, \mathbf{X}^3, \mathbf{X}^4\}) \quad (1)$$

where \mathbf{X}^i represents the i_{th} -level feature. $e(\cdot)$ and $d(\cdot)$ are two hypothetic function that can be approximated by the network with learning parameter θ_e and θ_d . This fused feature Z is finally classified by a segmentation head to output segmentation map.

Except for optimizing $e(\cdot)$ and $d(\cdot)$ from scratch, CL focuses on pre-training them with numerous unlabeled data to provide suitable initialization before supervised learning for downstream segmentation task. However, as shown in Figure 1(a), most existing CL frameworks [3]–[7] used for medical image segmentation are symmetric and similar to SimCLR [1], which only pre-trains an encoder $e(\cdot)$ with a global contrastive loss \mathcal{L}_g among image-level sample pairs:

$$\arg \min_{\theta_e} \mathcal{L}_g(e(\tilde{\mathbf{X}}), e(\hat{\mathbf{X}})) \quad (2)$$

where $\tilde{\mathbf{X}}$ and $\hat{\mathbf{X}}$ are two random augmentations of the input image \mathbf{X} . Apparently, the decoder structure $d(\cdot)$ is not considered in the above pre-training process, which ignores the importance of decoders to the downstream segmentation task. To solve this problem, as shown in Figure 1(b), GCL [7] proposes a two-stage CL framework which utilizes two pre-training stages to optimize $e(\cdot)$ with a global contrastive loss \mathcal{L}_g and $d(\cdot)$ with a local contrastive loss \mathcal{L}_l respectively:

$$\begin{cases} \arg \min_{\theta_e} \mathcal{L}_g(e(\tilde{\mathbf{X}}), e(\hat{\mathbf{X}})), & \text{in stage one} \\ \arg \min_{\theta_d} \mathcal{L}_l(d(e(\tilde{\mathbf{X}})), d(e(\hat{\mathbf{X}}))), & \text{in stage two} \end{cases} \quad (3)$$

where $\tilde{\mathbf{X}}$ and $\hat{\mathbf{X}}$ are two random augmentations of the input image \mathbf{X} , the parameters of $e(\cdot)$ are frozen in stage two. Although this strategy takes the decoder $d(\cdot)$ into consideration, the two-stage training process ignores the collaboration between the encoder and decoder during pre-training, which makes the decoder not able to learn image-level representation well due to the absence of global contrastive loss.

Based on the above issues, in order to realize the synchronous training of $e(\cdot)$ and $d(\cdot)$ to learn multi-level representations, we propose a novel one-stage multi-level asymmetric CL framework (MACL) shown in Figure 1(c). Our MACL framework pre-trains the encoder $e(\cdot)$ and decoder $d(\cdot)$ simultaneously with both image-level global contrastive loss \mathcal{L}_g and pixel-level dense contrastive loss \mathcal{L}_d to learn multi-level feature representations:

$$\arg \min_{\theta_e, \theta_d} \mathcal{L}_g(d(e(\tilde{\mathbf{X}})), d(e(\hat{\mathbf{X}}))) + \mathcal{L}_d(d(e(\tilde{\mathbf{X}})), d(e(\hat{\mathbf{X}}))) \quad (4)$$

where $\tilde{\mathbf{X}}$ and $\hat{\mathbf{X}}$ are two random augmentations of the input image \mathbf{X} . Our proposed MACL constructs a multi-level asymmetric CL framework which pre-trains the encoder and decoder simultaneously in one stage with a multi-level contrastive learning strategy. So both the encoder and decoder can synchronously learn multi-level representations and get better initialization.

B. Asymmetric CL Structure

In order to realize the one-stage synchronous training of encoder $e(\cdot)$ and decoder $d(\cdot)$ for better assisting the downstream segmentation tasks, our MACL elaborates an asymmetric CL structure as shown in Figure 2. This proposed structure contains two branches: (1) *dominant branch* which pre-trains both encoder and decoder simultaneously to get better initialization for downstream segmentation tasks and (2) *auxiliary branch* which serves as a contrastive counterpart to assist the dominant branch for pre-training.

Before being fed into the asymmetric CL structure, two different settings for data augmentations will be applied to the input image \mathbf{X} : (1) One set is only non-spatial augmentations T_{fix} which will be used for CL involving pixel-wise comparison including feature-level and pixel-level CL; (2) The other set is the combination of non-spatial and spatial augmentations T_{var} which is suitable for image-level CL not involving pixel-wise comparison:

$$\{\mathbf{I}_1, \mathbf{I}_2\} = T_{fix}(\mathbf{X}), \quad \{\mathbf{V}_1, \mathbf{V}_2\} = T_{var}(\mathbf{X}) \quad (5)$$

1) **Auxiliary Branch:** The auxiliary branch keeps in line with that of common CL strategies: an encoder $e(\cdot)$ followed by a shallow multi-layer perceptron (MLP) projection head $\tilde{g}(\cdot)$ [1] (but including an image-level projector $\tilde{g}_{ins}(\cdot)$ and pixel-level projector $\tilde{g}_{pix}(\cdot)$) and no decoder.

Specifically, the augmented image with pixel position fixed \mathbf{I}_2 is propagated to the encoder $e(\cdot)$ to get feature-level representation $\tilde{\mathbf{Y}}$ and then propagated into the pixel-level projector $\tilde{g}_{pix}(\cdot)$ to get pixel-level projection $\tilde{\mathbf{Z}}^l \in \mathbb{R}^{B \times C \times H \times W}$ (where B denotes batch size, C denotes channels, H denotes image height, W denotes image width):

$$\tilde{\mathbf{Y}} = e(\mathbf{I}_2), \quad \tilde{\mathbf{Z}}^l = \tilde{g}_{pix}(\tilde{\mathbf{Y}}) \quad (6)$$

While the augmented image with pixel position changed \mathbf{V}_2 is propagated into the encoder $e(\cdot)$ and the image-level projector $\tilde{g}_{ins}(\cdot)$ to get image-level projection $\tilde{\mathbf{Z}}^g \in \mathbb{R}^{B \times C}$:

$$\tilde{\mathbf{Z}}^g = \tilde{g}_{ins}(e(\mathbf{V}_2)) \quad (7)$$

2) **Dominant Branch:** Different from the auxiliary branch, the dominant branch introduces a decoder $d(\cdot)$ after the encoder $e(\cdot)$ for synchronous pre-training to dig more information from feature-level representation which is beneficial to the downstream segmentation tasks. The decoder $d(\cdot)$ is also followed by a MLP projection head $g(\cdot)$ (including an image-level projector $g_{ins}(\cdot)$ and pixel-level projector $g_{pix}(\cdot)$) as well). Moreover, due to the introduction of the decoder in this branch, the size of feature maps from two branches will be different if inputs are same. Hence, we add downsampling $down(\cdot)$ into data augmentation to align features which can also guarantee sufficient negative sample pairs due to its small computation complexity.

Specifically, the augmented image with pixel position fixed \mathbf{I}_1 is first downsampled, and then propagated to the encoder $e(\cdot)$ which shares the same parameters with that in the auxiliary branch to get the feature-level representation \mathbf{Y} and finally propagated to the decoder $d(\cdot)$ to recover image details which also serves as the pixel-level projection \mathbf{Z}^l :

$$\mathbf{Y} = e(down(\mathbf{I}_1)), \quad \mathbf{Z}^l = d(\mathbf{Y}) \quad (8)$$

While the augmented image with pixel position changed \mathbf{V}_1 is downsampled, propagated to the encoder $e(\cdot)$ and the image-level projector $g_{ins}(\cdot)$ to get image-level projection \mathbf{Z}^g :

$$\mathbf{Z}^g = g_{ins}(e(down(\mathbf{V}_1))) \quad (9)$$

With such a novel asymmetric network structure to guarantee the feature alignment between the representation output after $e(\cdot)$, $d(\cdot)$ in the dominant branch and that output after

$e(\cdot)$ in the auxiliary branch, we can realize one-stage synchronous training of $e(\cdot)$ and $d(\cdot)$ with more negative sample pairs and less computation complexity for better assisting the downstream segmentation tasks.

C. Multi-level CL Strategy

Under the guarantee of our proposed asymmetric CL structure in Section B which pre-trains the encoder and decoder simultaneously, we can optimize our MACL framework with multi-level contrastive learning strategy considering image-level, pixel-level and feature-level representations as follows:

$$\mathcal{L}_{MLC} = \lambda_1 \mathcal{L}_g + \lambda_2 \mathcal{L}_d + \lambda_3 \mathcal{L}_{ER} \quad (10)$$

where $\lambda_1, \lambda_2, \lambda_3$ are the weighting factors, and the overall pre-training is conducted in one-stage manner. We give the details of network training settings in Experimental Setup and carefully investigate the effectiveness of our MACL in different perspectives in Results and Discussions.

1) **Global Contrastive Learning:** The image-level representation is regulated by the global contrastive loss. Specifically, for a set of N randomly sampled slices: $\{X_i\}_{i=1\dots N}$, the corresponding mini-batch consists of $2N$ samples after data augmentations, $\{\tilde{X}_i\}_{i=1\dots 2N}$, in which \tilde{X}_{2i} and \tilde{X}_{2i-1} are two random augmentations of X_i . Z_i^g, \tilde{Z}_i^g represent the learned image-level projection of \tilde{X}_i from the dominant branch and auxiliary branch, respectively. Then the global contrastive loss can be formulated as:

$$\mathcal{L}_g = \sum_{i=1}^{2N} -\frac{1}{|\Omega_i^+|} \sum_{j \in \Omega_i^+} \log \frac{e^{sim(Z_i^g, \tilde{Z}_j^g)/\tau}}{\sum_{k=1}^{2N} \mathbb{I}_{i \neq k} \cdot e^{sim(Z_i^g, \tilde{Z}_k^g)/\tau}} \quad (11)$$

where $|\Omega_i^+|$ is the set of indices of positive samples to \tilde{X}_i . $sim(\cdot, \cdot)$ is the cosine similarity function that computes the similarity between two vectors in the representation space. τ is a temperature scaling parameter. \mathbb{I} is an indicator function. Compared with the standard contrastive loss [1] that only has one positive pair on the numerator for any sample X_i , we use the contrastive pair generation strategy in PCL [3] to form *position-based* positive and negative pairs.

2) **Dense Contrastive Learning:** The pixel-level representation is forced by our proposed dense contrastive loss which takes the correspondence between the pixel-level features into account and extends the original global contrastive loss to a dense paradigm. In detail, for a set of N randomly sampled slices: $\{X_i\}_{i=1\dots N}$, the corresponding mini-batch consists of $2N$ samples after data augmentation, $\{\tilde{X}_i\}_{i=1\dots 2N}$, in which \tilde{X}_{2i} and \tilde{X}_{2i-1} are two random augmentations of X_i . Different from the image-level projection Z_i^g and \tilde{Z}_i^g , Z_i^l and \tilde{Z}_i^l are pixel-level projections generated by the pixel-level projector in the dominant and auxiliary branch, respectively, which are dense feature maps with a size of $S \times S$. S denotes the spatial size of the generated dense feature maps. For every two input images, we can form S^2 pixel-level projection pairs (positive or negative pairs depending on Δ *position*) according to the *position-based* contrastive pair generation strategy. So the dense contrastive loss can be defined as:

$$\mathcal{L}_d = \sum_{i=1}^{2N} -\frac{1}{|\Omega_i^+|} \sum_{j \in \Omega_i^+} \frac{1}{S^2} \sum_s \log \frac{e^{\text{sim}(Z_{i,s}^l, \tilde{Z}_{j,s}^l)/\tau}}{\sum_{k=1}^{2N} \mathbb{1}_{i \neq k} e^{\text{sim}(Z_{i,s}^l, \tilde{Z}_{k,s}^l)/\tau}} \quad (12)$$

where $Z_{i,s}^l$ and $\tilde{Z}_{i,s}^l$ denote the s_{th} output of S^2 pixel-level projection pairs of \tilde{X}_i from the dominant branch and auxiliary branch, respectively.

3) Equivariant Regularization: The feature-level representation is governed by equivariant regularization [21]. Specifically, due to the introduction of downsampling in the dominant branch, the feature representations from the two encoders are different in size, therefore, we incorporate equivariant regularization into our multi-level CL to apply consistency regularization on multi-scale feature representations to provide further self-supervision for network learning. The equivariant regularization can be formulated as:

$$\mathcal{L}_{ER} = \|\mathbf{Y} - \text{down}(\tilde{\mathbf{Y}})\|_1 \quad (13)$$

where \mathbf{Y} and $\tilde{\mathbf{Y}}$ are the representations learned from the encoder in the dominant and auxiliary branch, respectively. We use L1 norm here to integrate consistency regularization on feature representations from the encoders to provide further self-supervision for network learning.

D. Experimental Setup

In order to verify the superiority of our proposed MACL framework, we conduct elaborate experiments between our MACL and other 11 CL methods across 12 datasets. And the experimental setup is detailed here.

Datasets: We evaluate the performance of our proposed MACL on two different types of segmentation tasks: Multi-organ segmentation and ROI (regions-of-interest, such as tumor, small objects, etc.) based segmentation. We use three publicly available medical image datasets for pre-training and twelve datasets for fine-tuning and evaluation of performance.

Multi-organ Segmentation: **(1) The CHD dataset** [22] is a CT dataset that consists of 68 3D cardiac images captured by a Siemens biograph 64 machine. The dataset covers 14 types of congenital heart disease and the segmentation labels include seven substructures: left ventricle (LV), right ventricle (RV), left atrium (LA), right atrium (RA), myocardium (Myo), aorta (Ao) and pulmonary artery (PA). **(2) The ACDC dataset** [23] has 100 patients with 3D cardiac MRI images and the segmentation labels include three substructures: LV, RV and Myo. **(3) The MMWHS dataset** [24] consists of 20 cardiac CT and 20 MRI images and the annotations include the same seven substructures as the CHD dataset. And we use the 20 cardiac CT images for fine-tuning. **(4) The HVSMR dataset** [25] has 10 3D cardiac MRI images captured in an axial view on a 1.5T scanner. Manual annotations of blood pool and Myo are provided. **(5) The CHAOS dataset** [26] has totally 120 DICOM datasets from T1-DUAL in/out phase and T2-SPIR. And we choose T2-SPIR train dataset with 20 DICOM MRI images and corresponding labels of four regions: liver, left kidney, right kidney and spleen for fine-tuning. **(6) The AMOS dataset** [27] has 100 3D MRI scans with voxel-level annotations of 15 abdominal organs. To ensure consistency, we

filter out those voxels with huge differences between length and width, and ultimately select 34 patients for fine-tuning.

ROI-based Segmentation: **(7) The BraTS2018 dataset** [28] contains a total of 351 patients scanned with T1, T1CE, T2, and Flair MRI volumes. And we choose 285 patients which are annotated with the segmentation labels including 3 tumor regions and 1 background region for pre-training. Notably, since there are no suitable large MRI datasets aimed for multi-organ segmentation, we use the BraTS2018 dataset as the pre-training dataset for both multi-organ and ROI-based MRI segmentation downstream tasks. **(8) The KiTS2019 dataset** [29] consists of 210 patients, aimed for kidney and kidney tumor segmentation and we choose it as the pre-training dataset for ROI-based CT segmentation. **(9) The MSD dataset** [30] has 10 available datasets, where each dataset has between one and three region-of-interest (ROI) targets. And we use three CT datasets: **Pancreas** (Task07, 281 patients labeled with pancreas and pancreatic tumor mass), **HepaticVessel** (Task08, 303 patients labeled with hepatic vessels and tumor), **Spleen** (Task09, 41 patients labeled with spleen) and three MRI datasets: **Heart** (Task02, 20 patients labeled with left atrium), **Hippocampus** (Task04, 260 patients labeled with anterior and posterior of hippocampus), **Prostate** (Task05, 32 patients labeled with prostate PZ and TZ) for fine-tuning.

Implementation Details: We employ our MACL framework to pre-train an U-Net encoder and two-block decoder on CHD, KiTS and BraTS dataset respectively without using any human label. Then the pre-trained model is used as the initialization to fine-tune an U-Net segmentation network (that is to say we add the remaining decoder blocks so that the output of the network has the same dimensions as the input) with a small number of labeled samples of 12 downstream datasets, respectively. Data pre-processing follows the same setting as PCL [3]. 5-fold cross-validation and commonly used Dice are used to evaluate the segmentation performance. Experiments of pre-training and fine-tuning are conducted with PyTorch on NVIDIA A100 GPUs. We find using the original images as spatial invariance group for calculating pixel-level CL loss has gained the best performance compared with using some non-spatial augmentations such as brightness, contrast, etc. Therefore, non-spatial augmentation is identity mapping, and spatial augmentations are translation, rotation and scale. In the pre-training stage, the weighted terms $\{\lambda_1, \lambda_2, \lambda_3\}$ are set to be $\{1.0, 0.5, 1.0\}$, temperature τ is set to be 0.1, the model is trained with 100 epochs, 16 batches per GPU, SGD optimizer and initial learning rate of 0.1, which is then decayed with the cosine scheduler on each training iterator. In the fine-tuning stage, we train the U-Net with cross-entropy loss for 100 epochs with Adam optimizer. The batch size per GPU is set to be 5, and initial learning rate is $5 \times e^{-4}$ which is decayed with cosine scheduler to minimum learning rate $5 \times e^{-6}$.

IV. RESULTS AND DISCUSSIONS

In this section, we evaluate the performance of our proposed MACL from quantitative and qualitative perspectives on the above datasets. Moreover, further ablation studies to verify the superiority and best parameters setting of our proposed MACL are also discussed.

TABLE I

QUANTITATIVE RESULTS OF OUR PROPOSED METHOD AGAINST OTHER SOTA METHODS ON MULTI-ORGAN SEGMENTATION TASK.

Methods	CHD (68 patients) [Dice (%)]				ACDC (100 patients) [Dice (%)]				MMWHS (20 patients) [Dice (%)]			
	$M = 6$	$M = 15$	$M = 51$	Average	$M = 3$	$M = 6$	$M = 10$	Average	$M = 6$	$M = 10$	$M = 16$	Average
Scratch	51.98	65.75	76.86	64.86	13.84	57.10	80.66	50.53	82.24	87.69	90.04	86.66
SimCLR [1]	52.48	66.31	76.24	65.01	16.90	54.60	75.78	49.09	81.29	87.25	89.80	86.11
MoCo [2]	50.77	65.19	75.99	63.98	11.06	47.57	78.09	45.57	80.47	86.95	89.61	85.68
BYOL [18]	51.16	64.98	76.89	64.34	15.25	57.44	81.68	51.46	81.96	87.68	89.88	86.51
SwAV [17]	50.37	65.52	77.21	64.37	14.18	59.44	80.15	51.26	81.73	86.95	89.61	86.10
SimSiam [19]	46.69	63.91	76.06	62.22	16.05	45.61	75.82	45.83	79.70	86.43	89.55	85.23
SimTriplet [6]	49.87	63.65	76.05	63.19	18.81	49.76	69.67	46.08	79.94	86.54	89.47	85.32
GCL [7]	52.97	66.43	77.08	65.43	33.52	75.66	82.71	63.96	81.07	87.91	90.02	86.33
PCL [3]	52.43	66.72	76.73	65.29	34.81	73.76	82.85	63.81	84.67	88.32	90.19	87.73
DeSD [4]	49.40	66.44	76.12	63.99	13.99	55.15	74.93	48.02	80.36	87.14	89.79	85.76
DiRA [5]	52.70	62.98	75.44	63.71	39.10	75.10	83.62	65.94	81.41	87.43	89.65	86.16
MACL (Ours)	56.87	68.98	77.29	67.71	68.35	82.87	85.89	79.04	86.69	89.71	90.76	89.05
Methods	HVSMR (10 patients) [Dice (%)]				CHAOS (20 patients) [Dice (%)]				AMOS (34 patients) [Dice (%)]			
	$M = 2$	$M = 4$	$M = 8$	Average	$M = 4$	$M = 12$	$M = 16$	Average	$M = 7$	$M = 10$	$M = 20$	Average
Scratch	76.27	82.57	84.36	81.07	64.37	82.76	84.73	77.29	20.21	35.26	49.30	34.92
SimCLR [1]	76.59	82.92	84.30	81.27	62.97	81.94	84.83	76.58	23.48	29.87	45.85	33.07
MoCo [2]	77.08	81.94	83.94	80.99	61.92	79.35	82.09	74.45	23.61	27.74	47.36	32.90
BYOL [18]	77.11	82.23	83.89	81.08	62.10	79.89	81.63	74.54	24.05	29.45	45.41	32.97
SwAV [17]	77.78	81.99	84.58	81.45	63.38	82.08	82.09	75.85	23.65	30.20	47.14	33.66
SimSiam [19]	75.74	79.26	82.97	79.32	47.33	72.63	75.18	65.05	21.75	26.26	45.33	31.11
SimTriplet [6]	76.72	80.91	83.18	80.27	49.93	73.09	79.50	67.51	21.91	24.81	44.84	30.52
GCL [7]	78.78	83.75	84.84	82.46	69.04	85.73	86.44	80.40	29.09	34.79	49.43	37.77
PCL [3]	78.11	83.98	85.32	82.47	69.21	84.52	87.15	80.29	28.33	35.15	49.16	37.55
DeSD [4]	78.43	82.59	84.30	81.77	64.74	82.23	83.91	76.96	24.22	29.70	45.40	33.11
DiRA [5]	77.06	82.15	85.05	81.42	58.26	83.25	85.34	75.62	27.88	34.07	49.08	37.01
MACL (Ours)	80.28	83.90	85.39	83.19	71.44	86.50	88.11	82.02	30.22	37.90	49.98	39.37

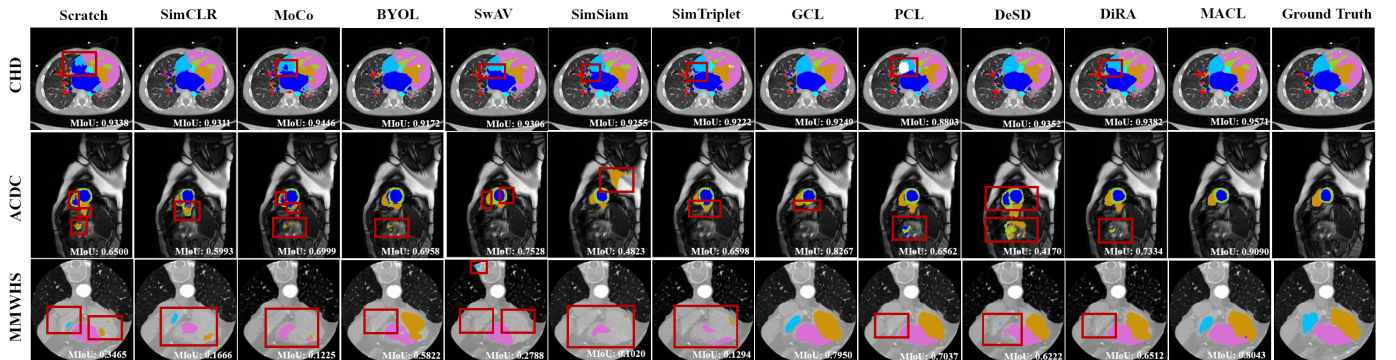


Fig. 3. Visualization of multi-organ segmentation results on CHD, ACDC and MMWHS datasets.

A. Results

Comparison Studies: We compare the performance of our MACL with the scratch approach which does not use any pre-training strategy as well as other state-of-the-art baselines, including 1) SimCLR [1], MoCo [2], BYOL [18], SwAV [17] and SimSiam [19] originally used in natural imaging domain but modified with an encoder of UNet as the backbone of CL; 2) SimTriplet [6], GCL [7], PCL [3], DeSD [4], DiRA [5] specially used in medical imaging domain. All the experiments across different methods have the same dataset settings and partition, and all the methods have the same backbone structures. The quantitative results carried on multi-organ and ROI-based segmentation task are shown in Table I and II. We report the averaged Dice of 5-fold cross-validation results.

Multi-organ Segmentation: From Table I, we have the following observations: (1) In general, benefited from our proposed asymmetric CL framework which pre-trains encoder and decoder simultaneously together with multi-level contrastive

learning, our MACL outperforms all the existing SOTA baselines in all values of M , *i.e.* 10% Dice higher than SimSiam on average when $M = 6$ of CHD and 29% Dice higher than DiRA when $M = 3$ of ACDC. (2) The performance improvement of our proposed MACL is high when a small number of training samples is used and the gains become lesser when the number of training samples increases. This is because with more training samples, the more supervisory information will be available, which results in that the improvement from self-supervised pre-training tends to saturate. And it can explain why our MACL is slightly superior to other baselines when M is maximum, and all the methods perform very closely. Moreover, the exemplar qualitative results of our MACL and 11 other methods on CHD, ACDC and MMWHS are shown in Figure 3. Red box indicates the wrong or missing predictions compared with the ground truth and it can be seen that our proposed method achieves a superior performance with a higher MIoU and more precise predictions of substructures across other 11 methods.

TABLE II

QUANTITATIVE RESULTS OF OUR PROPOSED METHOD AGAINST OTHER SOTA METHODS ON ROI-BASED SEGMENTATION TASK.

Methods	Task07 Pancreas (281 patients)				Task08 HepaticVessel (303 patients)				Task09 Spleen (41 patients)			
	[Dice (%)]				[Dice (%)]				[Dice (%)]			
Label fraction	10%	25%	50%	Average	10%	25%	50%	Average	10%	25%	50%	Average
Scratch	35.29	44.02	49.17	42.83	61.52	66.98	70.47	66.32	58.02	73.70	82.46	71.39
SimCLR [1]	36.13	44.89	49.01	43.34	62.10	67.42	69.91	66.48	63.95	77.27	80.48	73.90
SimTriplet [6]	28.79	35.82	43.36	35.99	59.84	65.46	68.98	64.76	57.86	75.32	81.25	71.48
GCL [7]	38.28	46.35	49.92	44.85	61.61	68.02	70.32	66.65	71.67	80.33	87.06	79.69
PCL [3]	37.72	46.33	50.14	44.73	61.64	68.06	70.50	66.73	71.57	78.55	84.48	78.20
DeSD [4]	35.53	44.56	48.15	42.75	61.22	67.58	70.27	66.36	60.83	69.39	82.00	70.74
DiRA [5]	33.44	40.66	46.37	40.16	61.16	67.26	69.98	66.13	64.39	74.85	82.55	73.93
MACL (Ours)	39.23	47.35	50.18	45.59	62.66	68.29	70.88	67.28	74.02	83.10	87.95	81.69
Methods	Task02 Heart (20 patients)				Task04 Hippocampus (260 patients)				Task05 Prostate (32 patients)			
	[Dice (%)]				[Dice (%)]				[Dice (%)]			
Label fraction	10%	25%	50%	Average	10%	25%	50%	Average	10%	25%	50%	Average
Scratch	68.02	83.33	87.30	79.55	78.54	84.08	86.23	82.95	30.17	46.88	54.59	43.88
SimCLR [1]	73.20	82.35	87.83	81.13	77.68	83.63	86.28	82.53	29.17	46.28	55.72	43.72
SimTriplet [6]	66.81	81.60	87.58	78.66	73.91	81.89	85.69	81.08	24.58	37.31	50.54	37.48
GCL [7]	76.67	83.65	87.37	82.56	78.19	83.56	86.37	82.71	29.48	47.26	55.14	43.96
PCL [3]	73.60	82.50	87.62	81.24	78.31	83.86	86.07	82.75	29.75	47.08	55.77	44.20
DeSD [4]	73.06	83.69	87.54	81.43	75.63	82.17	85.22	81.01	30.20	48.35	56.22	44.92
DiRA [5]	71.18	82.05	87.58	80.27	78.87	83.85	86.17	82.96	26.71	46.62	53.94	42.42
MACL (Ours)	76.12	84.18	88.13	82.81	78.92	84.10	86.38	83.13	30.24	51.51	57.64	46.46

TABLE III

THE ABLATION STUDIES FOR EACH COMPONENT OF OUR PROPOSED METHOD.

Framework	Settings					CHD [Dice (%)]		ACDC [Dice (%)]		MMWHS [Dice (%)]	
	\mathcal{L}_g	decoder	\mathcal{L}_{ER}	\mathcal{L}_d		$M = 6$	$M = 15$	$M = 3$	$M = 6$	$M = 6$	$M = 10$
PCL	✓					52.43	66.72	34.81	73.76	82.08	87.42
PCL + decoder	✓	✓				54.10	67.08	41.93	76.02	82.93	88.37
MACL (only image-level)	✓	✓	✓			54.75	67.53	59.22	80.26	84.93	88.73
MACL (image-level + pixel-level)	✓	✓	✓	✓	✓	56.87	68.98	68.35	82.87	86.69	89.71

ROI-based Segmentation: We further conduct more experiments on ROI-based segmentation task. Specifically, in terms of CT, we pre-train on KiTS dataset and fine-tune on Task07 Pancreas, Task08 Hepatic Vessel and Task09 Spleen, while as for MRI, we pre-train on BraTS dataset and fine-tune on Task02 Heart, Task04 Hippocampus and Task05 Prostate. We carry experiments on different label fractions including 10%, 25%, 50% and calculate the averaged dice among these three fractions for validation. From Table II, we can infer that our proposed MACL outperforms other medical CL methods in the majority of experiments and gains the highest averaged Dice among all the 6 datasets. Due to space limit, the visualization results of ROI-based segmentation are not presented here.

B. Discussions

Ablation Studies: Ablation studies have been conducted to verify the effectiveness of each part of our proposed components, *e.g.* the decoder structure, equivariant regularization \mathcal{L}_{ER} and dense contrastive loss \mathcal{L}_d of our proposed MACL framework. Results are reported in Table III. It can be seen that each part of our proposed components contributes to the improvement of performance. Specifically, the introduction of decoder structure and pixel-level dense contrastive loss \mathcal{L}_d improves the performance of our MACL framework to a greater extent compared with the slight promotion of equivariant regularization \mathcal{L}_{ER} , *i.e.* 1.7% and 1.5% Dice promotion when applying the decoder and \mathcal{L}_d respectively while 0.7% Dice promotion when applying \mathcal{L}_{ER} when $M = 6$ of CHD,

verifying the effectiveness of our proposed asymmetric CL structure and multi-level contrastive learning strategy.

Different connection modes of encoders: Considering there exists different connection modes of encoders in these SOTA methods, such as parameter-shared encoders in SimCLR and SimSiam, and encoder with EMA in MoCo and BYOL. We explore the performance of different connection modes of the encoder between two branches. From Table IV, we can conclude that the parameter-shared mode matters a lot especially in CL with negative sample pairs. Moreover, we further explore the performance between one-stage MACL (pre-train encoder and decoder simultaneously) and two-stage MACL (pre-train encoder and decoder separately). From Table IV, we can see that our MACL in one-stage setting performs much better than MACL in two stage setting (The connection mode of encoders in Stage two of Two-stage MACL is parameter-shared).

Encoder VS Encoder-Decoder: In order to validate our assumption: incorporating a decoder structure into CL framework for pre-training should also enhance the performance of downstream segmentation task, we make a comparison experiment: encoder (auxiliary branch of MACL) vs encoder-decoder (dominant branch of MACL). As shown in Table V, encoder-decoder structure outperforms only encoder structure. It can be expected that the performance of dominant branch will be better since additional well pre-trained decoder can better fuse multi-scale features and hence serves as a better initialization for UNet in downstream segmentation task.

Different numbers of blocks of decoder: We have also

TABLE IV

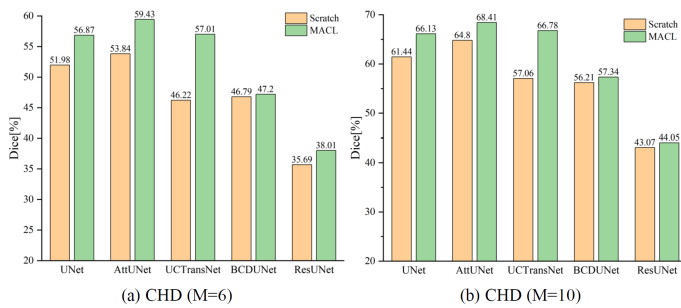
COMPARISON RESULTS OF DIFFERENT CONNECTION MODES OF ENCODERS AND DIFFERENT STAGES OF MACL.

	CHD (M=6)	
	Framework	Average Dice [%]
MACL(One Stage)	encoders with EMA	52.26
	two independent encoders	51.26
	two parameter-shared encoders	56.87
MACL(Two Stage)	stage one w downsample	52.78
	stage one w/o downsample	53.41

TABLE V

COMPARISON RESULTS OF FINE-TUNING DOWNSTREAM SEGMENTATION TASK BETWEEN ENCODER AND ENCODER-DECODER STRUCTURE.

Framework	Average Dice [%] ($M = 6$)	
	CHD	MMWHS
encoder+decoder (dominant branch)	56.87	86.69
encoder (auxiliary branch)	53.92	84.57

Fig. 4. Comparison results of different variants of UNet backbone on $M = 6$ and 10 of CHD dataset.

conducted an ablation study on the number of blocks ($N = 0,1,2,3,4$) of the decoder to verify the best number for choice. As shown in Table VI, all the frameworks with a decoder outperforms that without a decoder, and the two-block decoder gets the highest dice which is used as the baseline setting for other experiments. Since we need to add downsampling with a scale factor according to the numbers of blocks of the decoder, the input size is perhaps too small when three/four blocks of the decoder, resulting in a damage to image details and thus degrading performance.

Different forms of pixel-level dense contrastive loss: Before MLC loss of our proposed MACL is fully designed, we conduct a few comparison experiments between different forms of dense contrastive loss \mathcal{L}_d directly plugged into PCL, including MSE loss, BYOL-type loss (which is actually l_2 normalized + MSE used in BYOL) and SupConst loss (which is the form we end up using in our MACL). The results are shown in Table VII. It can be seen that SupConst form \mathcal{L}_d achieves the highest performance with Dice among all kinds of loss forms.

Variants U-Net backbones: The decoders used for medical image segmentation are usually U-shape, and our MACL can also be generalized to other variants of U-Net. We have conducted experiments on different variants of U-Net to verify generalization and universality of our proposed MACL. Specifically, we choose AttUNet [11] (decoder with attention blocks), UCTransNet [12] (Transformer complement to CNN-based U-Net), BCDUNet [13] (Bi-directional ConvLSTM U-Net with densely connected convolutions) and ResUNet [14]

TABLE VI

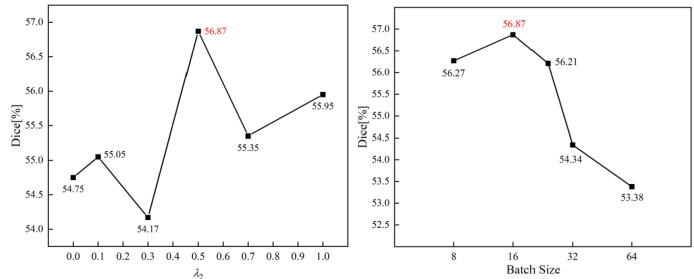
THE ABLATION STUDIES OF NUMBER OF BLOCKS OF THE DECODER. λ DENOTES SCALE FACTOR USED IN DOWNSAMPLING.

CHD (M=6)	
Number of Blocks	Average Dice [%]
0	52.43
1($\lambda = 0.5$)	56.11
2($\lambda = 0.25$)	56.87
3($\lambda = 0.125$)	55.43
4($\lambda = 0.0625$)	55.60

TABLE VII

COMPARISON RESULTS OF DIFFERENT FORMS OF PIXEL-LEVEL DENSE CONTRASTIVE LOSS ON CHD WITH $M=6$.

CHD ($M = 6$)	
Framework	Average Dice [%]
PCL (no \mathcal{L}_d)	52.43
PCL_MSE (MSE form \mathcal{L}_d)	54.68
PCL_BYOL (BYOL form \mathcal{L}_d)	51.64
PCL_SupConst (SupConst form \mathcal{L}_d)	55.00
MACL (Multi-level contrastive loss \mathcal{L}_{MLC})	56.87

Fig. 5. Comparison results of different λ_2 and batch size.

(U-Net with residual connections) for comparison with the basic U-Net [9]. The results are shown in Figure 4 and we can see that our MACL can be generalized to different model backbones. Specifically, AttUNet even outperforms basic UNet, and UCTransNet obtains an incredible improvement compared with that learning from scratch.

Ablation studies of λ_2 and batch size: According to Table III, we conclude that pixel-level dense CL loss \mathcal{L}_d matters more than equivariant regularization \mathcal{L}_{ER} , therefore we conduct a detailed ablation experiment of the weighted term λ_2 of \mathcal{L}_d . Moreover, we also verify the performance of our MACL among different batch size. From Figure 5, we conclude that $\lambda_2 = 0.5$ with batch size = 16 is the best setting which is also used as our baseline setting.

V. CONCLUSION

In this work, we propose a novel multi-level asymmetric CL framework named MACL for medical image segmentation pre-training. Specifically, we propose an asymmetric CL structure to pre-train both encoder and decoder simultaneously in one stage to provide better initialization for segmentation models. Additionally, We develop a multi-level contrastive learning strategy that integrates correspondences across feature-level, image-level, and pixel-level projections to ensure encoders and decoders capture comprehensive details from representations of varying scales and granularities during the pre-training

phase. Experiments on multiple datasets indicate our MACL outperforms existing SOTA CL methods.

REFERENCES

- [1] T. Chen, S. Kornblith, M. Norouzi, and G. Hinton, "A simple framework for contrastive learning of visual representations," in *International conference on machine learning*. PMLR, 2020, pp. 1597–1607.
- [2] K. He, H. Fan, Y. Wu, S. Xie, and R. Girshick, "Momentum contrast for unsupervised visual representation learning," in *Proceedings of the IEEE/CVF conference on computer vision and pattern recognition*, 2020, pp. 9729–9738.
- [3] D. Zeng, Y. Wu, X. Hu, X. Xu, H. Yuan, M. Huang, J. Zhuang, J. Hu, and Y. Shi, "Positional contrastive learning for volumetric medical image segmentation," in *International Conference on Medical Image Computing and Computer-Assisted Intervention*. Springer, 2021, pp. 221–230.
- [4] Y. Ye, J. Zhang, Z. Chen, and Y. Xia, "Desd: Self-supervised learning with deep self-distillation for 3d medical image segmentation," in *Medical Image Computing and Computer Assisted Intervention – MICCAI 2022*, L. Wang, Q. Dou, P. T. Fletcher, S. Speidel, and S. Li, Eds. Cham: Springer Nature Switzerland, 2022, pp. 545–555.
- [5] F. Haghighi, M. R. H. Taher, M. B. Gotway, and J. Liang, "Dira: Discriminative, restorative, and adversarial learning for self-supervised medical image analysis," in *Proceedings of the IEEE/CVF Conference on Computer Vision and Pattern Recognition (CVPR)*, June 2022, pp. 20 824–20 834.
- [6] Q. Liu, P. C. Louis, Y. Lu, A. Jha, M. Zhao, R. Deng, T. Yao, J. T. Roland, H. Yang, S. Zhao *et al.*, "Simtriplet: Simple triplet representation learning with a single gpu," in *Medical Image Computing and Computer Assisted Intervention–MICCAI 2021: 24th International Conference, Strasbourg, France, September 27–October 1, 2021, Proceedings, Part II 24*. Springer, 2021, pp. 102–112.
- [7] K. Chaitanya, E. Erdil, N. Karani, and E. Konukoglu, "Contrastive learning of global and local features for medical image segmentation with limited annotations," *Advances in Neural Information Processing Systems*, vol. 33, pp. 12 546–12 558, 2020.
- [8] J. Long, E. Shelhamer, and T. Darrell, "Fully convolutional networks for semantic segmentation," in *Proceedings of the IEEE conference on computer vision and pattern recognition*, 2015, pp. 3431–3440.
- [9] O. Ronneberger, P. Fischer, and T. Brox, "U-net: Convolutional networks for biomedical image segmentation," in *Medical image computing and computer-assisted intervention–MICCAI 2015: 18th international conference, Munich, Germany, October 5–9, 2015, proceedings, part III 18*. Springer, 2015, pp. 234–241.
- [10] L.-C. Chen, Y. Zhu, G. Papandreou, F. Schroff, and H. Adam, "Encoder-decoder with atrous separable convolution for semantic image segmentation," in *Proceedings of the European conference on computer vision (ECCV)*, 2018, pp. 801–818.
- [11] O. Oktay, J. Schlemper, L. L. Folgoc, M. Lee, M. Heinrich, K. Misawa, K. Mori, S. McDonagh, N. Y. Hammerla, B. Kainz *et al.*, "Attention u-net: Learning where to look for the pancreas," *arXiv preprint arXiv:1804.03999*, 2018.
- [12] H. Wang, P. Cao, J. Wang, and O. R. Zaiane, "Uctransnet: rethinking the skip connections in u-net from a channel-wise perspective with transformer," in *Proceedings of the AAAI conference on artificial intelligence*, vol. 36, no. 3, 2022, pp. 2441–2449.
- [13] R. Azad, M. Asadi-Aghbolaghi, M. Fathy, and S. Escalera, "Bi-directional convlstm u-net with densley connected convolutions," in *Proceedings of the IEEE/CVF international conference on computer vision workshops*, 2019, pp. 0–0.
- [14] M. Drozdal, E. Vorontsov, G. Chartrand, S. Kadoury, and C. Pal, "The importance of skip connections in biomedical image segmentation," in *International workshop on deep learning in medical image analysis, international workshop on large-scale annotation of biomedical data and expert label synthesis*. Springer, 2016, pp. 179–187.
- [15] F. Isensee, P. F. Jaeger, S. A. Kohl, J. Petersen, and K. H. Maier-Hein, "nnu-net: a self-configuring method for deep learning-based biomedical image segmentation," *Nature methods*, vol. 18, no. 2, pp. 203–211, 2021.
- [16] A. v. d. Oord, Y. Li, and O. Vinyals, "Representation learning with contrastive predictive coding," *arXiv preprint arXiv:1807.03748*, 2018.
- [17] M. Caron, I. Misra, J. Mairal, P. Goyal, P. Bojanowski, and A. Joulin, "Unsupervised learning of visual features by contrasting cluster assignments," *Advances in neural information processing systems*, vol. 33, pp. 9912–9924, 2020.
- [18] J.-B. Grill, F. Strub, F. Althé, C. Tallec, P. Richemond, E. Buchatskaya, C. Doersch, B. Avila Pires, Z. Guo, M. Gheshlaghi Azar *et al.*, "Bootstrap your own latent—a new approach to self-supervised learning," *Advances in neural information processing systems*, vol. 33, pp. 21 274–21 284, 2020.
- [19] X. Chen and K. He, "Exploring simple siamese representation learning," in *Proceedings of the IEEE/CVF conference on computer vision and pattern recognition*, 2021, pp. 15 750–15 758.
- [20] Á. S. Hervella, L. Ramos, J. Rouco, J. Novo, and M. Ortega, "Multi-modal self-supervised pre-training for joint optic disc and cup segmentation in eye fundus images," in *ICASSP 2020-2020 IEEE international conference on acoustics, speech and signal processing (ICASSP)*. IEEE, 2020, pp. 961–965.
- [21] Y. Wang, J. Zhang, M. Kan, S. Shan, and X. Chen, "Self-supervised equivariant attention mechanism for weakly supervised semantic segmentation," in *Proceedings of the IEEE/CVF Conference on Computer Vision and Pattern Recognition*, 2020, pp. 12 275–12 284.
- [22] X. Xu, T. Wang, Y. Shi, H. Yuan, Q. Jia, M. Huang, and J. Zhuang, "Whole heart and great vessel segmentation in congenital heart disease using deep neural networks and graph matching," in *Medical Image Computing and Computer Assisted Intervention–MICCAI 2019: 22nd International Conference, Shenzhen, China, October 13–17, 2019, Proceedings, Part II 22*. Springer, 2019, pp. 477–485.
- [23] O. Bernard, A. Lalande, C. Zotti, F. Cervenansky, X. Yang, P.-A. Heng, I. Cetin, K. Lekadir, O. Camara, M. A. Gonzalez Ballester, G. Sanroma, S. Napel, S. Petersen, G. Tziritas, E. Grinias, M. Khened, V. A. Kollerathu, G. Krishnamurthi, M.-M. Rohé, X. Pennec, M. Sermesant, F. Isensee, P. Jäger, K. H. Maier-Hein, P. M. Full, I. Wolf, S. Engelhardt, C. F. Baumgartner, L. M. Koch, J. M. Wolterink, I. Išgum, Y. Jang, Y. Hong, J. Patravali, S. Jain, O. Humbert, and P.-M. Jodoin, "Deep learning techniques for automatic mri cardiac multi-structures segmentation and diagnosis: Is the problem solved?" *IEEE Transactions on Medical Imaging*, vol. 37, no. 11, pp. 2514–2525, 2018.
- [24] X. Zhuang, "Challenges and methodologies of fully automatic whole heart segmentation: a review," *Journal of healthcare engineering*, vol. 4, no. 3, pp. 371–407, 2013.
- [25] D. F. Pace, A. V. Dalca, T. Geva, A. J. Powell, M. H. Moghari, and P. Golland, "Interactive whole-heart segmentation in congenital heart disease," in *Medical Image Computing and Computer-Assisted Intervention–MICCAI 2015: 18th International Conference, Munich, Germany, October 5–9, 2015, Proceedings, Part III 18*. Springer, 2015, pp. 80–88.
- [26] A. E. Kavur, N. S. Gezer, M. Barış, S. Aslan, P.-H. Conze, V. Groza, D. D. Pham, S. Chatterjee, P. Ernst, S. Özkan, B. Baydar, D. Lachinov, S. Han, J. Pauli, F. Isensee, M. Perkonig, R. Sathish, R. Rajan, D. Sheet, G. Dovletov, O. Speck, A. Nürnberg, K. H. Maier-Hein, G. Bozdağı Akar, G. Ünal, O. Dicle, and M. A. Selver, "CHAOS Challenge - combined (CT-MR) healthy abdominal organ segmentation," *Medical Image Analysis*, vol. 69, p. 101950, Apr. 2021. [Online]. Available: <http://www.sciencedirect.com/science/article/pii/S1361841520303145>
- [27] Y. Ji, H. Bai, C. Ge, J. Yang, Y. Zhu, R. Zhang, Z. Li, L. Zhanng, W. Ma, X. Wan *et al.*, "Amos: A large-scale abdominal multi-organ benchmark for versatile medical image segmentation," *Advances in Neural Information Processing Systems*, vol. 35, pp. 36 722–36 732, 2022.
- [28] S. Bakas, M. Reyes, A. Jakab, S. Bauer, M. Rempfler, A. Crimi, R. T. Shinohara, C. Berger, S. M. Ha, M. Rozycski *et al.*, "Identifying the best machine learning algorithms for brain tumor segmentation, progression assessment, and overall survival prediction in the brats challenge," *arXiv preprint arXiv:1811.02629*, 2018.
- [29] N. Heller, F. Isensee, K. H. Maier-Hein, X. Hou, C. Xie, F. Li, Y. Nan, G. Mu, Z. Lin, M. Han *et al.*, "The state of the art in kidney and kidney tumor segmentation in contrast-enhanced ct imaging: Results of the kits19 challenge," *Medical image analysis*, vol. 67, p. 101821, 2021.
- [30] M. Antonelli, A. Reinke, S. Bakas, K. Farahani, A. Kopp-Schneider, B. A. Landman, G. Litjens, B. Menze, O. Ronneberger, R. M. Summers *et al.*, "The medical segmentation decathlon," *Nature communications*, vol. 13, no. 1, p. 4128, 2022.